J. Fluid Mech. (2008), *vol.* 604, *pp.* 33–53.
doi:10.1017/S0022112008001304 Printed in the United Kingdom

Numerical analysis of two-dimensional motion of a freely falling circular cylinder in an infinite fluid

KAK NAMKOONG[1], JUNG YUL YOO[2] AND HYOUNG G. CHOI[3]†

[1]Bio & Health Laboratory, Samsung Advanced Institute of Technology, San 14-1, Nongseo-dong, Giheung-gu, Yongin-si, Gyeonggi-do 446-712, Korea

[2]School of Mechanical and Aerospace Engineering, Seoul National University, San 56-1, Shinlim-dong, Kwanak-gu, Seoul 151-744, Korea

[3]Department of Mechanical Engineering, Seoul National University of Technology, 172, Gongreung-2-dong, Nowon-gu, Seoul 139-743, Korea

(Received 4 July 2007 and in revised form 30 January 2008)

The two-dimensional motion of a circular cylinder freely falling or rising in an infinite fluid is investigated numerically for the range of Reynolds number $Re < 188$ (Galileo number $G < 163$), where the wake behind the cylinder remains two-dimensional, using a combined formulation of the governing equations for the fluid and the dynamic equations for the cylinder. The effect of vortex shedding on the motion of the freely falling or rising cylinder is clearly shown. As the streamwise velocity of the cylinder increases due to gravity, the periodic vortex shedding induces a periodic motion of the cylinder, which is manifested by the generation of the angular velocity vector of the cylinder parallel to the cross-product of the gravitational acceleration vector and the transverse velocity vector of the cylinder. Correlations of the Strouhal–Reynolds-number and Strouhal–Galileo-number relationship are deduced from the results. The Strouhal number is found to be smaller than that for the corresponding fixed circular cylinder when the two Reynolds numbers based on the streamwise terminal velocity of the freely falling or rising circular cylinder and the free-stream velocity of the fixed one are the same. From numerical experiments, it is shown that the transverse motion of the cylinder plays a crucial role in reducing the Strouhal number. The effect of the transverse motion is similar to that of suction flow on the low-pressure side, where a vortex is generated and then separates, so that the pressure on this side recovers with the vortex separation retarded. The effects of the transverse motion on the lift, drag and moment coefficients are also discussed. Finally, the effect of the solid/fluid density ratio on Strouhal–Reynolds-number relationship is investigated and a plausible correlation is proposed.

1. Introduction

Since Strouhal (1878) first measured the vortex shedding frequency in the wake of a circular cylinder, the flow around a circular cylinder has been the subject of numerous studies. Notably, Lord Rayleigh (1945) put forward a functional relationship between

† Author to whom correspondence should be addressed: hgchoi@snut.ac.kr

a frequency parameter (now called the Strouhal number, St) and a viscosity parameter (the inverse of what is now called the Reynolds number, Re). Recent developments in the understanding of wake vortex dynamics were extensively reviewed by Williamson (1996). In addition to the flows around a fixed circular cylinder, the flows around an oscillating or rotating cylinder have also been studied extensively after it was found that the self-excitation by the fluid motion was the main reason for the breakup of Tacoma bridge (Billah & Scanlan 1991).

The closely related subject of the flow around a freely falling sphere or clusters of spheres has been investigated by many researchers. Karamanev & Nikolov (1992) conducted an experiment on the motion of a freely rising or falling sphere in distilled water. They claimed that the trajectory of either a rising or falling sphere was a vertical straight line when the terminal Reynolds number is smaller than 130 or the particle density is larger than $0.9\,\mathrm{g\,cm^{-3}}$. Karamanev, Chavarie & Mayer (1996) studied the change in the drag coefficient between a very light particle ($\rho_s \sim 0.3\,\mathrm{g\,cm^{-3}}$) and a particle with density close to that of water. They showed that the particle trajectory is a spiral and the Strouhal number based on a characteristic length scale of the spiral motion of a rising sphere is comparable to that of the flow around a fixed sphere when the terminal velocity of the particle is over $14.5\,\mathrm{cm\,s^{-1}}$.

More recent numerical and experimental studies on the flow around a sphere have focused on detailed flow characteristics that depend on the Galileo number and the density ratio of the sphere to the surrounding fluid. Jenny, Bouchet & Dušek (2003) studied a regular, symmetry-breaking bifurcation of the flow around a freely falling or ascending sphere in a Newtonian fluid by using the spectral-spectral-element method. In their study, two independent dimensionless parameters, the Galileo number and the density ratio, were introduced and they showed that the trajectory of the regular bifurcation is characterized by steady oblique straight lines. They successfully conducted a direct numerical simulation of very light particles using a fully implicit algorithm which couples the motion equation of a sphere with the time-stepping algorithm of the Navier–Stokes equation. As a result of the explicit treatment of the nonlinear terms of the Navier–Stokes equations, the Stokes-like equations were solved for the flow field. Thus, the coupling of the motion of the sphere with the flow field could be achieved in an efficient manner by utilizing the linearity of the Stokes equation (Jenny & Dušek 2004). By extending the numerical results of the primary bifurcation (Jenny *et al.* 2003), Jenny, Dušek & Bouchet (2004) studied the secondary, Hopf bifurcation using two, dimensionless parameters the solid/fluid density ratio and the Galileo number. An experimental verification of the numerical study of Jenny *et al.* (2004) was conducted recently by Veldhuis & Biesheuvel (2007). In those studies, a diagram of the instability and transition of a falling or ascending sphere was obtained for a wide range of the density ratio and the Galileo number, and the regimes are classified into steady and oblique, oblique and oscillating, zigzagging periodic and three-dimensional chaotic. One of striking differences between the numerical study and the experimental study is that the experimental trajectory of a falling sphere may be non-vertical as the Reynolds number increases (Veldhuis *et al.* 2005). This is not consistent with the claim of Jenny *et al.* (2004) that only ascending spheres can have a zigzagging motion.

According to the experimental study on a rising or falling cylinder by Horowitz & Williamson (2006), the amplitude of the transverse motion of a falling cylinder is about 5 % of the diameter of the cylinder when the density ratios are about 1.4 and 2.0. Although the amplitude data for small density differences (small Reynolds numbers less than 200) are not given in the paper, presumably because a very long

distance is necessary for a falling cylinder to enter a periodic mode, the amplitude data from Horowitz & Williamson (2006) are comparable to those of the present two-dimensional numerical study. They also showed that a rising cylinder experiences a sudden jump in the amplitude of transverse motion for a density ratio of less than 0.54.

A numerical computation of the two-dimensional flow around a freely falling circular cylinder in a channel was performed by Hu, Joseph & Crochet (1992), Feng, Hu & Joseph (1994) and Choi (2000). Hu *et al.* (1992)and Choi (2000), who studied the sedimentation due to gravity of a circular cylinder in a channel, reported that the vortex shedding frequency, i.e. St, becomes smaller than that associated with the flow around a fixed circular cylinder. However, it was not elucidated whether this phenomenon is due to the existence of channel walls (Chen, Pritchard & Tavener 1995; Zovatto & Pedrizzetti 2001) or the motion of the cylinder.

In view of all the previous studies, there is a need for further investigations on the two-dimensional flow around a freely falling or rising circular cylinder in an infinite fluid. The vortex shedding will induce some motion of the cylinder, which in turn will affect the flow field. It appears that St for the flow around a freely falling or rising circular cylinder in an infinite fluid will be affected by the motion of the cylinder due to the vortex shedding. Thus, the objective of the present paper is to investigate the two-dimensional flow around a freely falling or rising circular cylinder. The relationship between Re and St is obtained for small density difference, and compared with that for the flow around a fixed circular cylinder. In the case of large density difference, a new formula representing the effect of the solid/fluid density ratio and the Reynolds number on the Strouhal number is proposed. Furthermore, the interactions between the cylinder and fluid motions are investigated by applying various combinations of constraints on the rotational and translational degrees of freedom of the cylinder.

2. Numerical method

In order to solve the present problem, a combined finite-element formulation based on the P2P1 Galerkin method and ALE technique (Choi 2000; Hu, Patankar & Zhu 2001) is adopted to describe the motion of the cylinder, in combination with the solution of the Navier–Stokes equations. In this combined formulation, the motion of the cylinder is coupled with the flow variables (pressure and velocity fields) via the hydrodynamic force and moment acting on the cylinder. Therefore, a global matrix containing both flow variables and velocity components of the cylinder is constructed. Since the bandwidth of the global matrix is very large owing to the coupling of the cylinder motion with the flow variables, an effective preconditioning method has to be employed to solve the global matrix by an iterative solver. In the present study, the Bi-CGSTAB iterative solver with an AILU (Adapted Incomplete LU)-type preconditioner for the combined finite-element formulation based on the P2P1 Galerkin method is adopted for this purpose. The preconditioner is an extended version of the AILU preconditioning method for the incompressible Navier–Stokes equations (Nam, Choi & Yoo 2002). For fully resolved numerical solutions with an efficient distribution of nodes of an unstructured mesh around the single cylinder, an adaptive mesh refinement technique (Nithiarasu & Zienkiewicz 2000), which is based on the error estimation of the shear-stress field, has been used. A more detailed description of the numerical methods used in the present study is given in the Appendix.

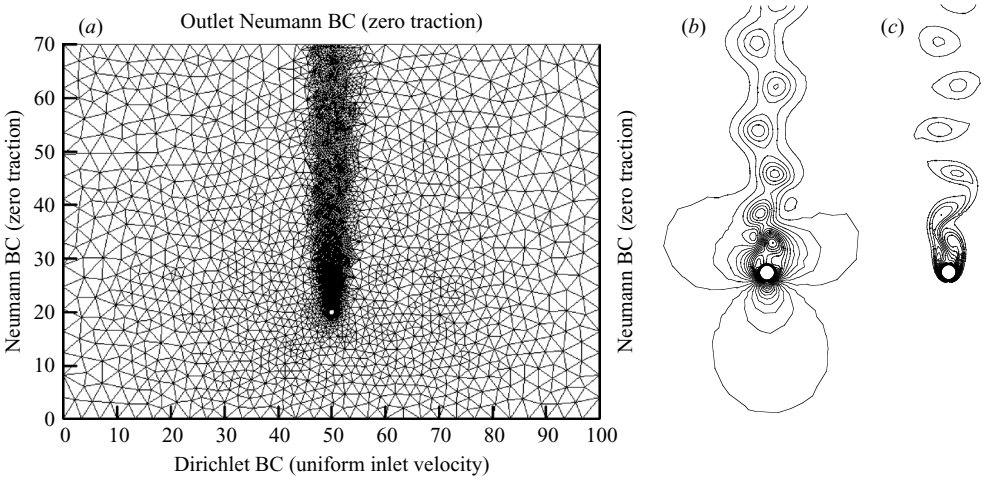

FIGURE 1. (*a*) Computational mesh and boundary conditions, (*b*) instantaneous pressure contours, and (*c*) instantaneous vorticity contours at $Re = 100$ for a fixed cylinder.

3. Results

3.1. *Two-dimensional laminar flow around a fixed circular cylinder*

For the validation of the adaptive finite-element code developed in the present study, two-dimensional laminar flow around a fixed circular cylinder is tested. The wake flow behind a fixed circular cylinder is known to remain two-dimensional when the Reynolds number, $Re = U_\infty D/\nu_f$, based on the free-stream velocity U_∞, the cylinder diameter D, and the kinematic viscosity of fluid ν_f, is lower than a certain critical value, about 190 (Henderson 1997; Williamson & Brown 1998). In this section, two-dimensional numerical simulations are performed at six different Reynolds numbers, $Re = 60$, 80, 100, 120, 140, and 160. The computational mesh and boundary conditions are shown in figure 1(*a*). The size of the computational domain has been set to $70D$ in the streamwise direction ($20D$ in front of the cylinder centre and $50D$ behind) and $100D$ in the transverse direction ($50D$ on both left and right sides of the cylinder centre). The dimensionless time step ($\Delta t U_\infty/D$) is 0.05 for all cases. The total of numbers nodes, vertex nodes, and elements are 25 386, 6401, and 12 584, respectively, after 29 mesh refinements. Instantaneous pressure contours and vorticity contours at $Re = 100$ are shown in figure 1(*b*) and figure 1(*c*), respectively, where the typical wake pattern due to periodic vortex shedding is clearly seen. The Strouhal number ($St = fD/U_\infty$, where f is the vortex shedding frequency) is calculated as $St = 0.1653$, which is in good agreement with the value in the literature. The relation between St and Re is plotted and compared with the experimental results of Fey, König & Eckelmann (1998) and Williamson & Brown (1998) in figure 2 where one can see good agreement again. Fey *et al.* (1998) and Williamson & Brown (1998) proposed the following formula for the relation between St and Re:

$$St = A + \frac{B}{\sqrt{Re}}, \tag{3.1}$$

where A is related related to the size or physical shape of the body and $B/\sqrt{Re}$ is associated with the shear layer thickness (Williamson & Brown 1998). The constants A and B in equation (3.1) are found to be 0.2672 and -1.0162, respectively, both of which are very close to those of Williamson & Brown (1998) ($A = 0.2665$ and

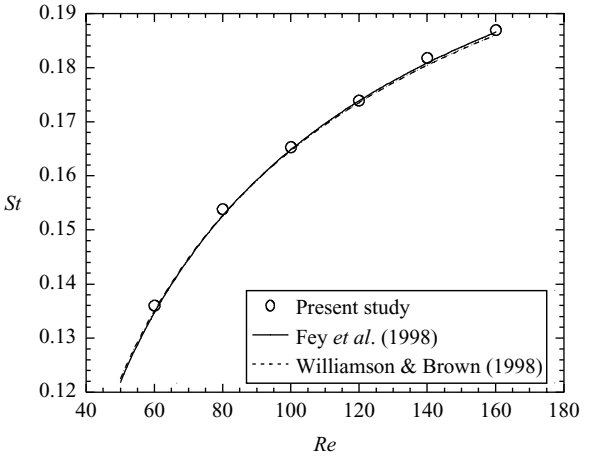

FIGURE 2. *St–Re* relation for two-dimensional laminar flow around a fixed circular cylinder, compared with other experimental results.

	$\Delta t = 0.02$ s	$\Delta t = 0.01$ s	$\Delta t = 0.005$ s	$\Delta t = 0.0025$ s
Mesh I	0.186 cm s^{-1} (0.18572)	0.201 cm s^{-1} (0.18549)	0.210 cm s^{-1} (0.18535)	0.212 cm s^{-1} (0.18530)
Mesh II	0.187 cm s^{-1} (0.18572)	0.201 cm s^{-1} (0.18549)	0.210 cm s^{-1} (0.18535)	—
Mesh III	0.187 cm s^{-1} (0.18572)	0.201 cm s^{-1} (0.18549)	—	—

TABLE 1. Dependence of the maximum transverse velocity (Strouhal number) on time-step size and grid resolution at $\rho_s/\rho_f = 1.010$ and $G = 138$ ($Re = 156$).

$B = -1.0180$) and Fey *et al.* (1998) ($A = 0.2684$ and $B = -1.0356$). Therefore, it can be said that the present adaptive code based on h-refinement is efficient in accurately resolving the wake flow behind a blunt body.

3.2. *Spatial and temporal resolution test*

In order to prove that the present two-dimensional combined solutions are grid and time-step independent, spatial and temporal resolution tests were conducted, where the density of the freely falling cylinder is 1.01 times that of the surrounding fluid (water). The Reynolds number based on the terminal velocity of the cylinder and the cylinder diameter is 156. As shown in table 1, four time-step sizes and three different unstructured meshes consisting of P2P1 triangular elements are used in order to compare the maximum transverse velocity and the Strouhal number during periodic motion. At the initial stage of computation, Meshes I, II and III are generated by placing 64, 80 and 96 nodes on the particle surface, respectively. In the course of the computation, the mesh adaption described in the Appendix is applied wherever necessary. At the final stage of computation after adaption, the numbers of nodes for Meshes I, II and III are 29 125, 40 893 and 42 799, respectively. Table 1 shows that the present numerical results are more dependent on the time-step size than on the type of mesh used. Therefore, Mesh I with the time-step size of 0.005 s is adopted for all the simulations of the present study. It should be also noted that the maximum difference in the Strouhal number is less than 0.2 % for the results given in table 1.

3.3. *Two-dimensional motion of a freely falling or rising circular cylinder in an infinite fluid with small density difference*

Assuming that the wake flow behind a freely falling or rising circular cylinder remains two-dimensional over approximately the same Re range as that behind a fixed circular cylinder, two-dimensional numerical simulations were performed at seven different Reynolds numbers, based on the streamwise terminal velocity U_t, the cylinder diameter D, and the kinematic viscosity of the fluid ν_f, i.e. $Re = U_t D/\nu_f = 66$, 96, 119, 138, 156, 171 and 185. Both the fluid and the cylinder are initially at rest and the cylinder is set into free-fall or free-rise motion abruptly due to gravity in an infinite fluid for $t \geqslant 0$ s. Note that the Reynolds number is not an independent variable but dependent on the Galileo number $G(=(|\rho_s/\rho_f - 1|gD^3)^{1/2}/\nu_f)$ and the density ratio ρ_s/ρ_f, where ρ_s, ρ_f, g represent the density of the cylinder, the density of the fluid and the magnitude of gravitational acceleration, respectively. Therefore, the Reynolds numbers we investigate are obtained by keeping fixed the density of the fluid, the gravitational acceleration, and the diameter of the cylinder such that $\rho_f = 0.996\,\mathrm{g\,cm^{-3}}$, $D = 0.5$ cm, and $g_x = -981\,\mathrm{cm\,s^{-2}}$, and varying the density of the cylinder such that $\rho_s/\rho_f = 1.002$, 1.004, 1.006, 1.008, 1.010, 1.012 and 1.014 for the falling cases and $\rho_s/\rho_f = 0.998$, 0.996, 0.994, 0.992, 0.990, 0.988, 0.986 for the rising cases. Cases for $\rho_s/\rho_f > 1.014$ and $\rho_s/\rho_f < 0.986$ are discarded because the Reynolds numbers exceed the two-dimensional wake flow limit, i.e. $Re > 190$ (Henderson 1997; Williamson & Brown 1998). The Galileo numbers corresponding to respective Reynolds numbers, $G(Re)$ are 62(66), 87(96), 107(119), 123(138), 138(156), 151(171), 163(185) in both falling and rising cases, so that the Galileo number is linearly related to the Reynolds number: $G = 0.851Re + 5.547$.

Time histories of the translational velocity components and angular velocity of the freely falling cylinder at $\rho_s/\rho_f = 1.010$ and $G = 138$ ($U_t = 2.501\,\mathrm{cm\,s^{-1}}$ and $Re = 156$) are shown in figure 3, where U_p and V_p are the streamwise and transverse velocity components of the cylinder in the x- and y-directions, respectively, and ω_p is the angular velocity of the cylinder. For $tU_t/D > 60$, the motion of the cylinder is almost periodic. Note that the total cylinder velocity is almost the same as U_p due to the very small contribution of V_p. A schematic illustrating the motion of the freely falling cylinder in an infinite fluid is shown in figure 4, which shows that when the cylinder falls rotating in the positive z-direction it moves in the negative y-direction and vice versa. That is, the direction of the angular velocity vector ω of the falling cylinder is given by the cross-product of the gravitational acceleration and the velocity vector in the transverse direction:

$$\boldsymbol{\omega} // (\boldsymbol{g} \times \boldsymbol{V}). \tag{3.2}$$

It is noteworthy that equation (3.2) is in accordance with the Bernoulli theorem, as will be seen in detail later (see figures 6*a* and 7).

For a freely falling or rising cylinder, the Strouhal number is defined as $St = fD/U_t$, where f is the vortex shedding frequency or oscillation frequency of the lift force. The St–Re and St–G relations for the freely falling and rising cylinders with small density difference are shown in figure 5(*a*), where one can see that the relations for the freely rising cylinder are the same as for the freely falling cylinder within computational error. While a falling cylinder and a rising cylinder with the same density difference have the same magnitude of driving force (gravity minus buoyant force), the mass of the rising cylinder is smaller than that of the falling cylinder (refer to equation (A 6) in the Appendix). Thus, the rising cylinder tends to move more violently than the falling cylinder when the density difference is the same. As will be revealed in § 3.4 on

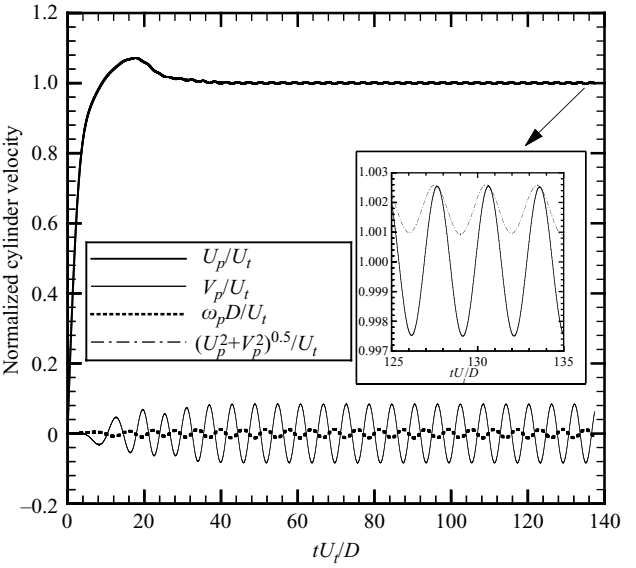

FIGURE 3. Time histories of streamwise and transverse velocity components (U_p and V_p) and angular velocity (ω_p) of the freely falling cylinder, where U_t is the streamwise terminal velocity of the cylinder: $\rho_s/\rho_f = 1.01$, $G = 138$, $Re = 156$, $U_t = 2.501\,\mathrm{cm\,s^{-1}}$. Note that the total magnitude of the cylinder velocity is almost the same as U_p due to the very small contribution of V_p.

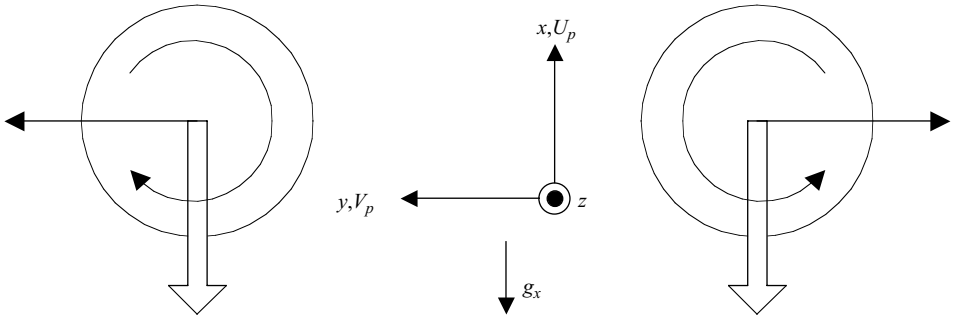

FIGURE 4. Schematic illustrating the motion of the freely falling cylinder.

the effect of a large density difference, the motion of the rising cylinder is different from that of the falling cylinder even when the absolute magnitude of the density difference is the same, although the St–G relation of the present section turns out to be nearly the same for both a falling cylinder and a rising cylinder with the same absolute magnitude of the density difference. The St–Re relation for the freely falling cylinder obtained by curve-fitting using equation (3.1) is shown in figure 5(*b*). The result of Williamson & Brown (1998) for the flow around a fixed circular cylinder is also shown for comparison. It is apparent that St for the freely falling circular cylinder is smaller than for the fixed circular cylinder when Re based on the terminal velocity of the freely falling circular cylinder and that based on the free-stream velocity of the fixed circular cylinder are the same. The constants A and B in equation (3.1) are found to be 0.2404 and -0.9078, respectively, both of which are lower than those of

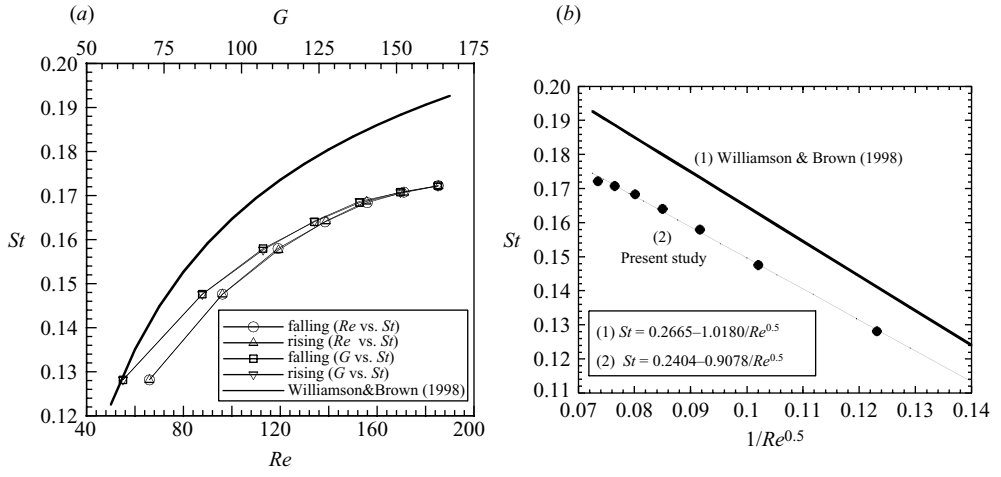

FIGURE 5. (*a*) *St*–*Re* and *St*–*G* relation in a laminar flow around a freely falling or rising circular cylinder and (*b*) *St* vs. $1/Re^{0.5}$. The result of Williamson & Brown (1998) for the laminar flow around a fixed circular cylinder is also shown for comparison.

Direction of motion	Falling							Rising		Fixed
Constraints	010	011	110	111	001	100	101	111	101	000
St	0.1659	0.1673	0.1676	0.1684	0.1860	0.1843	0.1847	0.1687	0.1842	0.1868

TABLE 2. *St* from 'numerical experiments' with eight different combinations of constraints at $\rho_s/\rho_f = 1.010$ and $G = 138$ ($Re = 156$).

Williamson & Brown (1998) ($A = 0.2665$ and $B = -1.0180$). The same form of the correlation between the Strouhal number and the Galileo number can be found by curve-fitting: $St = 0.2458 - 0.9187/G^{0.5}$. The reason for these reduced *St* values could be only that the cylinder is free to move in the present study.

To understand this more physically, 'numerical experiments' are carried out at the same *Re* as in figure 3, but with constraints placed on rotational and/or translational degrees of freedom of the cylinder motion. Specifically, we denote a free-to-move state of a velocity component by '1' and a frozen state by '0'. With this notation, we can make eight different combinations of constraints on (U_p, V_p, ω_p): (111) – unconstrained motion; (110) – $\omega_p = 0$, U_p and V_p unconstrained; (101) – $V_p = 0$, U_p and ω_p unconstrained; (100) – $V_p = \omega_p = 0$, U_p unconstrained; (011) – $U_p =$ constant, V_p and ω_p unconstrained; (010) – $U_p =$ constant, $\omega_p = 0$, V_p unconstrained; (001) – $U_p =$ constant, $V_p = 0$, ω_p unconstrained; (000) – $U_p =$ constant, $V_p = \omega_p = 0$. The flow field of (000) is the same as a uniform flow around a fixed cylinder after a Galilean transformation. The results of these 'numerical experiments' are given in table 2. Note that only for the combinations (101), (100) and (001) are *St* values as high as that for the fixed circular cylinder, and those for the combinations (111), (110), (011) and (010) are smaller than that for the fixed circular cylinder. This result suggests that the transverse motion of the cylinder plays a crucial role in reducing *St* for the laminar flow around the freely falling circular cylinder, while the rotation of

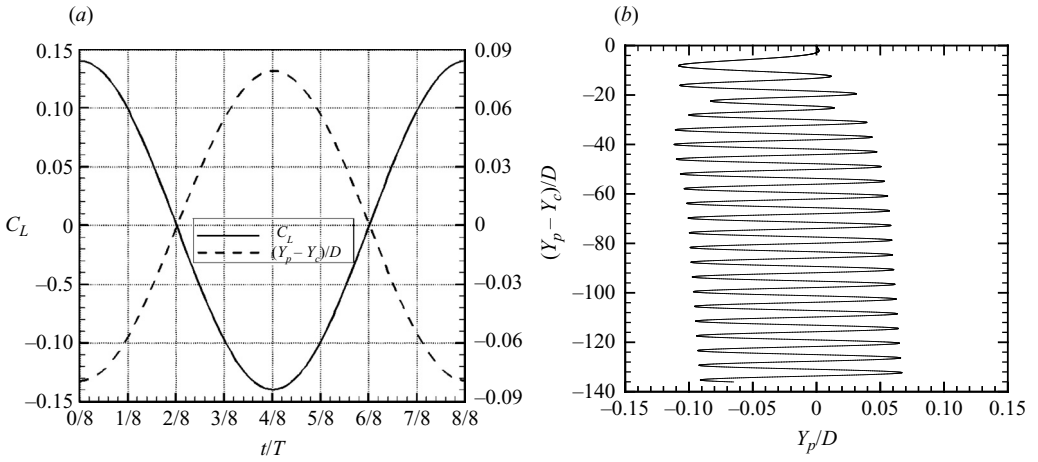

FIGURE 6. (*a*) Time histories of the lift coefficient and the transverse position Y_p during 1 period, where Y_c denotes the mid-point position of the cylinder in the transverse direction, and (*b*) two-dimensional trajectory up to $tU_t/D \approx 140$ of the freely falling cylinder at $\rho_s/\rho_f = 1.010$ and $G = 138$ ($Re = 156$). For convenience, the phases where the snapshots of figure 7 are taken are indicated along the abscissa in figure 6(*a*).

the freely falling cylinder has a negligible effect on the reduction of St. This is also the case for the freely rising cylinders as can be seen from table 2.

Because St represents the frequency of vortex shedding, the fact that it is reduced means that the vortex shedding is retarded. The time histories of the resultant lift coefficient C_L ($=Lift/(0.5\rho_f U_t^2 D)$) and the corresponding transverse position Y_p of the cylinder at $\rho_s/\rho_f = 1.010$ and $G = 138$ ($Re = 156$) are shown on figure 6(*a*). For $0 < t < (4/8)T$, the cylinder moves towards its maximum transverse position $(Y_p)_{\max}$ while the lift force approaches its minimum value. Note that vortex shedding occurs on the left ($+y$) side at $t = (2/8)T$, when the cylinder is located transversely at the mid-point ($0^- \to 0^+$) and the lift force is zero ($0^+ \to 0^-$). After this vortex shedding, the cylinder moves transversely beyond the mid-position until $(Y_p)_{\max}$ is reached at $t = (4/8)T$. The reason for the turning of the cylinder into the $-y$ direction at $t = (4/8)T$ is that after the vortex shedding on the left ($+y$) side at $t = (2/8)T$, a vortex starts to roll up on the right ($-y$) side, where the local pressure is smaller than the surroundings, such that the cylinder moves in the $-y$ direction. For $(4/8)T < t < (8/8)T$, the cylinder moves towards its minimum transverse position $(Y_p)_{\min}$ while the lift force approaches its maximum value. It can be easily deduced that the phase difference between C_L and Y_p should be 180°, which corresponds to the two-dimensional wake flow at $Re < 190$ and a harmonic oscillation of the cylinder with small density difference. The amplitude of the transverse motion of the cylinder is found to be small, $0.08D$. Another vortex shedding occurs on the right ($-y$) side at $t = (6/8)T$, when the cylinder is located transversely at the mid-point ($0^+ \to 0^-$) and the lift force is zero again ($0^- \to 0^+$). After this vortex shedding, the cylinder moves transversely past the mid-position until $(Y_p)_{\min}$ is reached at $t = (8/8)T$. Corresponding to the previous shedding, the reason for the turn of the cylinder in the $+y$ direction at $t = (8/8)T$ is that after the vortex shedding on the right ($-y$) side at $t = (6/8)T$, a vortex starts to roll up on the left ($+y$) side, where the local pressure is smaller than the surroundings, so that the cylinder moves in the $+y$ direction.

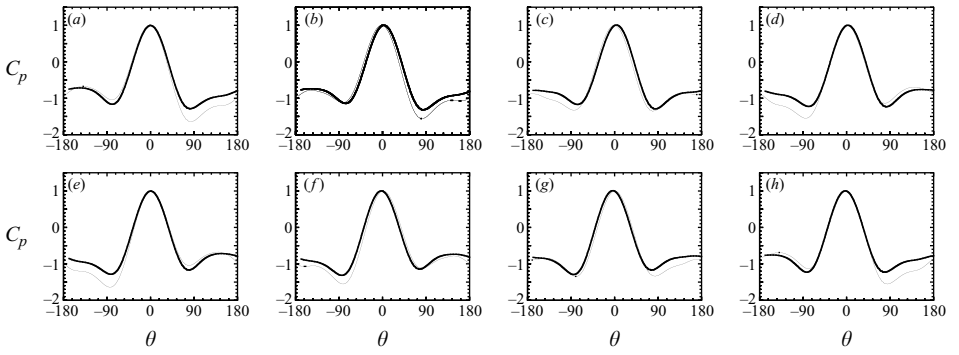

FIGURE 7. Snapshots of the instantaneous pressure coefficients on the cylinder surface taken for one period of vortex shedding in the flow around the freely falling circular cylinder at $\rho_s/\rho_f = 1.010$ and $G = 138$ ($Re = 156$). Those for the fixed circular cylinder at $Re = 156$ are also shown for comparison: —, freely falling cylinder; —, fixed cylinder. (*a*) $t/T = 0/8$, (*b*) 1/8, (*c*) 2/8, (*d*) 3/8, (*e*) 4/8, (*f*) 5/8, (*g*) 6/8, (*h*) 7/8.

The two-dimensional trajectory of the cylinder up to $tU_t/D \approx 140$ at the same conditions as in figure 6(*a*) is shown in figure 6(*b*), where the motion of the cylinder is found to be oblique and periodically oscillating. It is noted that the non-dimensional spatial amplitude of the transverse motion of a freely falling cylinder with small density difference, i.e. $\rho_s/\rho_f \leqslant 1.014$, is given by the following formula: $A_m/D = 0.034 + 3.38 \times 10^{-4} G$ with $R^2 = 0.99566$.

Snapshots of the instantaneous pressure coefficients along the cylinder surface at the same conditions as in figure 6(*a*) are shown as thick lines over one period of vortex shedding in figure 7, where those for the fixed circular cylinder at $Re = 156$ obtained in the present study are also shown as thin lines for comparison. The angle θ in figure 7 is measured from the stagnation point and is positive in the clockwise direction and negative in the counter-clockwise direction. That is, it is positive on the left ($+y$) surface and negative on the right ($-y$) surface of the cylinder. The pressure coefficients in figure 7 are calculated using the following equation:

$$C_p = \frac{p - (p_s + 0.5\rho_f U^2)}{0.5\rho_f U^2} = \frac{p - p_s}{0.5\rho_f U^2} + 1, \tag{3.3}$$

where p_s is the pressure at the stagnation point ($\theta = 0$) and U is the free-stream velocity (U_∞) in the fixed cylinder case and the terminal velocity (U_t) in the freely falling cylinder case. At almost all times and along the cylinder surface for $|\theta| > 40°$, the pressure coefficients of the freely falling cylinder are negative but smaller in magnitude than those of the fixed cylinder.

The time-averaged pressure coefficients at $\rho_s/\rho_f = 1.010$ and $G = 138$ ($Re = 156$) along the surface of the freely falling circular cylinder for the eight different combinations of constraints in the numerical experiments are shown in figure 8, where that of the fixed cylinder at $Re = 156$ is also shown for comparison. One can clearly see the effect of the transverse motion of the cylinder. That is, the pressure coefficients without the transverse motion are nearly the same as that for the fixed cylinder, while those with the transverse motion have a smaller magnitude in the negative region ($|\theta| > 40°$) than that for the fixed cylinder. A free-fall cylinder without any transverse constraint will tend to translate to the low-pressure side, where a vortex begins to roll up and then separate. This tendency turns out to be similar

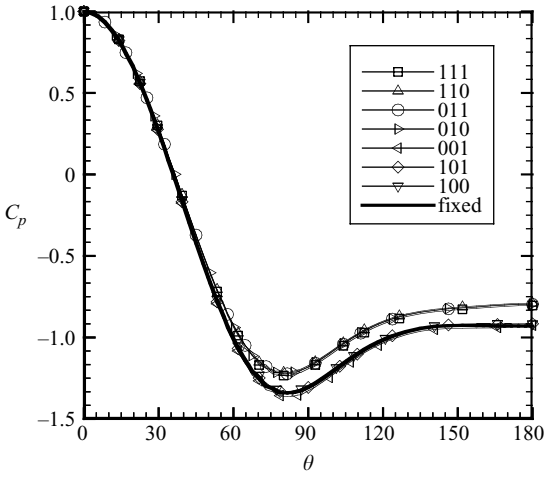

FIGURE 8. Time-averaged pressure coefficients along the surface of the freely falling circular cylinder for the eight different combinations of constraints at $\rho_s/\rho_f = 1.010$ and $G = 138$ ($Re = 156$). The pressure coefficient for the fixed circular cylinder at $Re = 156$ is also shown for comparison.

to the existence of suction flow on the low-pressure side such that the pressure on this side recovers with the vortex separation retarded. Consequently, St of the freely falling cylinder is reduced in comparison with that of the fixed cylinder case owing to the transverse motion.

Figure 9 provides a comparison of the average drag coefficients ($C_D = Drag/(0.5\rho_f U_t^2 D)$), the amplitudes of the lift coefficient (C_L), moment coefficients ($C_T = Moment/(0.5\rho_f U_t^2 D^2)$), and the amplitudes of angular oscillation for the eight different combinations of constraints in the numerical experiments. It is shown that the lift coefficients with transverse motion are reduced to approximately 1/4 of those without transverse motion and that the drag coefficients with transverse motion are about 8 % less than those without transverse motion. It is remarkable that the moment coefficients do not follow the pattern of drag and lift coefficients in the dependence on the transverse motion but depend on the combination of transverse and angular oscillations. In fact, C_T increases in the order (111), (011), (101), (001), (110), (010), (100) and (000) and it is physically reasonable that the angular constraint should give a higher C_T than the transverse constraint. However, constraint of U_p seems to have little effect on C_T as can be clearly seen by comparing cases (111) and (011). The same is true for the cases (101) and (001), (110) and (010), and (100) and (000) cases. C_T of a fixed cylinder is more than double that of a freely falling cylinder. As shown in figure 9(*d*), the amplitude of angular oscillation is very small, which can be conjectured from the fact that the rotational motion of a freely falling cylinder has a negligible effect on the reduction of the Strouhal number (table 2).

3.4. *The effect of large density difference*

In the previous section, the Galileo number was the primary parameter in describing the motion of the cylinders. However, as mentioned in Introduction, the motion of a freely falling or rising cylinder in an infinite fluid is governed by two dimensionless parameters, the Galileo number and the solid/fluid density ratio (Jenny *et al.* 2004). In this section, cases with wider range of the density ratio, i.e. $0.5 \leqslant \rho_s/\rho_f \leqslant 4.0$ are investigated.

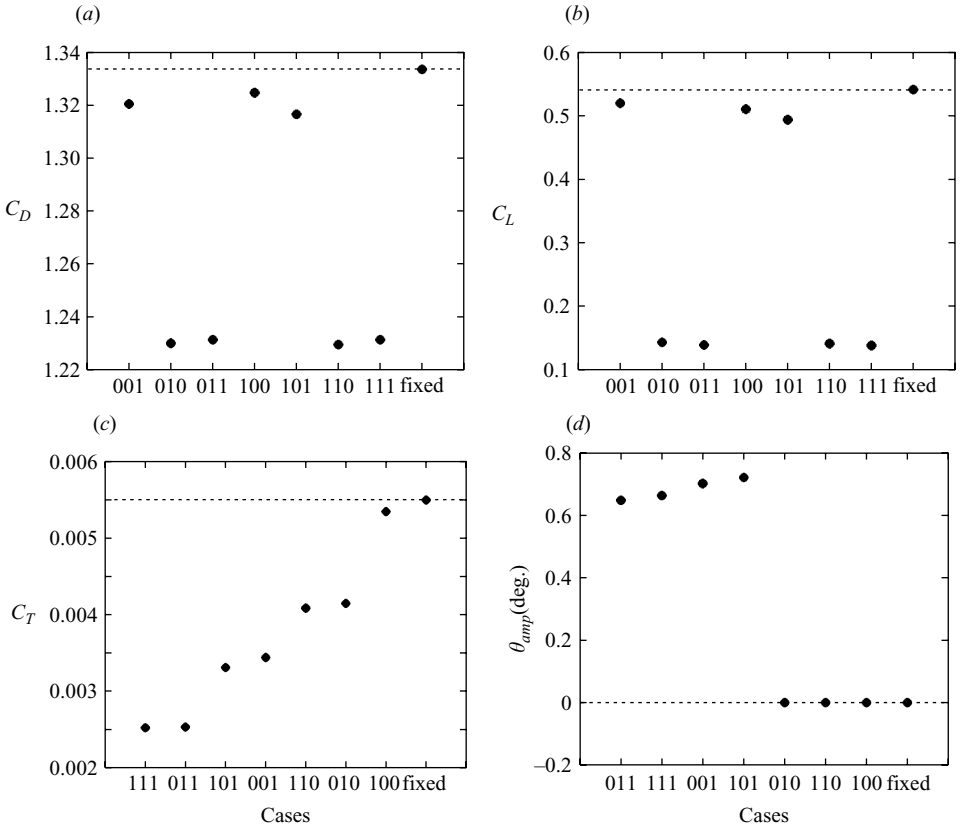

FIGURE 9. Comparison of (*a*) the average drag coefficients, (*b*) the amplitudes of lift coefficients, (*c*) the amplitudes of moment coefficients, and (*d*) the amplitudes of angular oscillation of the freely falling cylinder for the eight different combinations of constraints at $\rho_s/\rho_f = 1.010$ and $G = 138$ ($Re = 156$).

$G = 62$			$G = 107$			$G = 151$			$G = 163$		
ρ_s/ρ_f	Re	St	ρ_s/ρ_f	Re	St	ρ_s/ρ_f	Re	St	ρ_s/ρ_f	Re	St
0.50	66.3	0.1226	0.50	120.5	0.1540	1.10	170.3	0.1718	0.50	187.9	0.1677
0.85	65.9	0.1270	0.85	119.4	0.1570	1.20	170.0	0.1723	0.70	186.2	0.1699
1.25	65.8	0.1298	1.25	118.8	0.1595	1.30	169.9	0.1729	0.80	185.5	0.1709
1.40	65.8	0.1306	1.40	118.6	0.1601	1.40	169.6	0.1735	0.90	184.8	0.1720
						2.00	168.5	0.1761			
						4.00	166.8	0.1801			

TABLE 3. St and Re for a wide range of the solid/fluid density ratio and the Galileo number.

To see the effect of the density ratio, the following 18 cases are considered: (G, ρ_s/ρ_f) = (62, 0.50), (62, 0.85), (62, 1.25), (62, 1.40), (107, 0.50), (107, 0.85), (107, 1.25), (107, 1.40), (151, 1.10), (151, 1.20), (151, 1.30), (151, 1.40), (151, 2.00), (151, 4.00), (163, 0.50), (163, 0.70), (163, 0.80), (163, 0.90). The Strouhal numbers from all the above cases are shown in table 3, where it is easily seen that St increases linearly with the density ratio when the Galileo number is fixed. Considering the fixed cylinder case as a limiting one of $\rho_s/\rho_f \to \infty$ and the linearly increasing relation of St to ρ_s/ρ_f, the

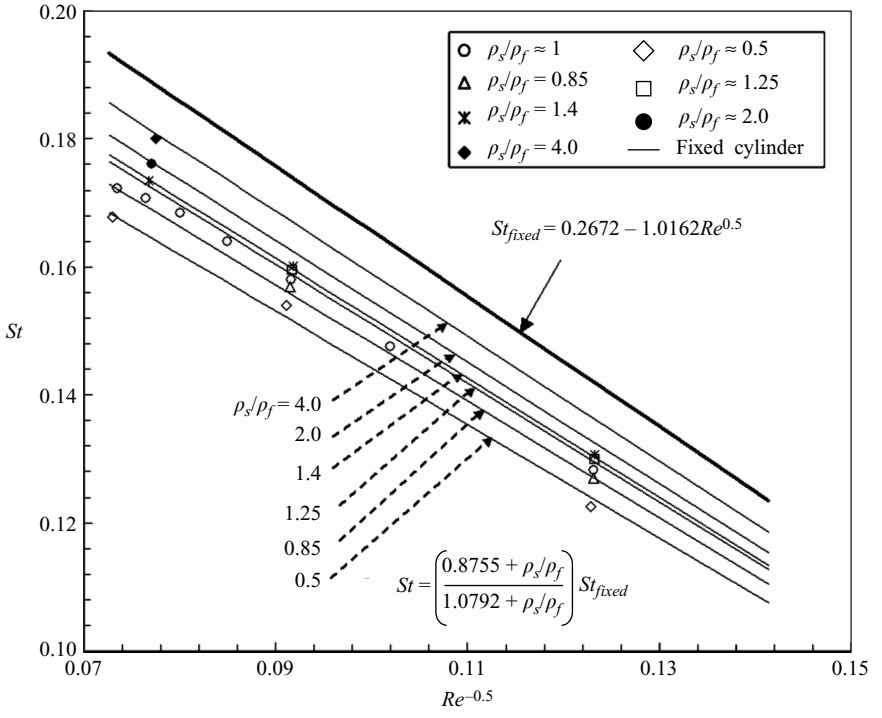

FIGURE 10. Effect of the solid/fluid density ratio on the *St*–*Re* relation in a laminar flow around a freely falling or rising circular cylinder. The thick line corresponds to the fixed cylinder case obtained from the present calculation, while the thin lines represent equation (3.4) for $\rho_s/\rho_f = 0.5$, 0.85, 1.25, 1.4, 2.0 and 4.0.

following equation is formulated for $St = f(\rho_s/\rho_f, Re)$:

$$St = \left(\frac{\rho_s/\rho_f + A}{\rho_s/\rho_f + B}\right) St_{fixed} = \left(\frac{\rho_s/\rho_f + A}{\rho_s/\rho_f + B}\right) (0.2672 - 1.0162/Re^{0.5}), \qquad (3.4)$$

where A and B are constants and $St_{\text{fixed}} = 0.2672 - 1.0162Re^{-0.5}$ represents the *St*–*Re* relation for a fixed circular cylinder in a two-dimensional wake flow, obtained in § 3.1. The constants A and B are found to be 0.8755 and 1.0792, respectively, from the Levenberg–Marquardt method with $R^2 = 0.99795$. Equation (3.4) and St–$Re^{-0.5}$ data for $\rho_s/\rho_f = 0.5$, 0.85, 1.25, 1.4, 2.0 and 4.0 are shown in figure 10, where results for a small density difference ($\rho_s/\rho_f \approx 1$) of § 3.3 are also shown. It is easily seen that equation (3.4) is an excellent candidate for representing $St = f(\rho_s/\rho_f, Re)$ for the two-dimensional motion of a freely falling or rising circular cylinder in an infinite fluid. As the solid/fluid density ratio increases, the Strouhal number also increases and the freely falling cylinder has a higher Strouhal number than the freely rising one when the Reynolds numbers are the same.

4. Concluding remarks

The flow around a freely falling or rising circular cylinder in an infinite fluid has been investigated using an adaptive P2P1 finite-element formulation based on *h*-refinement, and a combined formulation of the governing equations for the fluid and the dynamic equations for the cylinder. From the present study, the following conclusions can be drawn.

1. The present adaptive code based on h-refinement is efficient in accurately resolving the wake flow behind a blunt body. The predicted St–Re relationship is very accurate with a reasonable number of nodes compared with the previous results.

2. The direction of the angular velocity vector $\boldsymbol{\omega}$ of the falling cylinder in infinite fluid is given by the cross-product of the gravitational acceleration and the velocity vector in the transverse direction, which is in accordance with the Bernoulli theorem.

3. From numerical experiments, it has been found that the reduction of St for the freely falling cylinder is attributed to the transverse motion of the cylinder. A freely falling cylinder without any transverse constraint will tend to translate to the low-pressure side, where a vortex begins to roll up and then separate. This motion has a similar effect as the existence of suction flow on the low-pressure side so that the pressure on this side recovers with the vortex separation retarded. Consequently, St of the freely falling cylinder is reduced compared to that of the fixed cylinder owing to the transverse motion.

4. It has been found that the non-dimensional spatial amplitude of the transverse motion of a freely falling cylinder with small density difference, i.e. $\rho_s/\rho_f \leqslant 1.014$, has the following linear relationship with the Galileo number: $A_m/D = 0.034 + 3.38 \times 10^{-4} G$.

5. Owing to pressure recovery on the low-pressure side by the transverse motion, a freely falling cylinder experiences a smaller lift than a fixed cylinder at the corresponding Reynolds number. The maximum drag coefficient of the freely falling cylinder is also smaller than that of the fixed cylinder since the freely falling cylinder tends to move to a low-pressure region by the transverse motion. The moment coefficient C_T increases in the order (111), (011), (101), (001), (110), (010), (100) and (000) of constraint combinations and the angular constraint gives a higher C_T than the transverse constraint. C_T of a fixed cylinder is more than double that of a freely falling cylinder.

6. As the solid/fluid density ratio increases, the Strouhal number of a freely falling or rising cylinder also increases so that the freely falling cylinder has a higher Strouhal number than the freely rising one when the Reynolds numbers are the same. The effect of the solid/fluid density ratio and the Reynolds number on the Strouhal number for a freely falling or rising cylinder is correlated well with the following formula: $St = (\rho_s/\rho_f + A)/(\rho_s/\rho_f + B) \times St_{\text{fixed}}$.

H. G. C. was supported by the Korea Science and Engineering Foundation (KOSEF) grant (No. R01-2006-000-11122-0), subsidized by the Ministry of Science and Technology (MOST), and J. Y. Y. by Micro Thermal System Research Center at Seoul National University under the auspices of KOSEF.

Appendix. Numerical method

A. 1. Governing equation for fluid and P2P1 Galerkin formulation

The governing equations for an incompressible flow with moving boundaries are the Navier–Stokes equations and the continuity equation as follows:

$$\rho_f \left(\frac{\partial \boldsymbol{u}}{\partial t} + \{(\boldsymbol{u} - \boldsymbol{u}_m) \cdot \nabla\} \boldsymbol{u} \right) = \nabla \cdot \tilde{\boldsymbol{\sigma}} \quad \text{where} \quad \tilde{\boldsymbol{\sigma}} = -p\tilde{\boldsymbol{I}} + \tilde{\boldsymbol{\tau}}, \quad \tilde{\boldsymbol{\tau}} = \mu\{\nabla \boldsymbol{u} + (\nabla \boldsymbol{u})^{\mathrm{T}}\}. \tag{A 1}$$

$$\nabla \cdot \boldsymbol{u} = 0, \tag{A 2}$$

where $\boldsymbol{u}$ is the velocity vector, $\boldsymbol{u}_m$ is the mesh velocity, $\tilde{\boldsymbol{\sigma}}$ is the stress tensor, p is the pressure, $\tilde{\boldsymbol{\tau}}$ is the shear stress tensor which is linearly related to the deformation tensor in the Newtonian fluid, and μ is the dynamic viscosity of fluid. The boundary conditions are as follows:

$$\left.\begin{aligned} \boldsymbol{u} &= \boldsymbol{U} \quad \text{on} \quad \Gamma_g, \\ \tilde{\boldsymbol{\sigma}} \cdot \boldsymbol{n} &= -p\boldsymbol{n} + \mu \left[\nabla \boldsymbol{U} + (\nabla \boldsymbol{U})^{\mathrm{T}} \right] \cdot \boldsymbol{n} \quad \text{on} \quad \Gamma_h, \end{aligned}\right\} \tag{A 3}$$

where Γ_g is the part of the boundary where the Dirichlet boundary condition for velocity ($\boldsymbol{g}$) is prescribed, Γ_h is the other part of the boundary where the Neumann boundary condition for velocity ($\boldsymbol{h}$) is prescribed.

In the FSI problems, the interface between the fluid and the structure often changes in time and the computational domain should be changed accordingly. To do this, we use the ALE technique. In the ALE technique, the mesh velocity $\boldsymbol{u}_m$ is obtained by solving the following Laplace equation:

$$\nabla \cdot (\nabla \boldsymbol{u}_m) = 0 \tag{A 4}$$

Applying the P2P1 Galerkin finite element method to equation (A 1) and equation (A 2) and invoking the divergence theorem, we arrive at the following weak formulation:

Find $\boldsymbol{u} \in H^1(\Omega)$, $p \in L^2(\Omega)$ *such that*

$$\int_\Omega \left[\boldsymbol{W} \cdot \rho_f \left(\frac{\partial \boldsymbol{u}}{\partial t} + \{(\boldsymbol{u} - \boldsymbol{u}_m) \cdot \nabla\} \boldsymbol{u} \right) + \nabla \boldsymbol{W} : \tilde{\boldsymbol{\sigma}} \right] \mathrm{d}\Omega - \oint_\Gamma \boldsymbol{W} \cdot (\tilde{\boldsymbol{\sigma}} \cdot \boldsymbol{n}) \mathrm{d}\Gamma + \int_\Omega q \, (\nabla \cdot \boldsymbol{u}) \, \mathrm{d}\Omega = 0 \tag{A 5}$$

for all admissible functions $\boldsymbol{W} \in V$, $q \in P$

where $V = \{\boldsymbol{W} | \boldsymbol{W} \in H^1(\Omega),\ \boldsymbol{W} = \boldsymbol{0}$ *on* $\Gamma_g\}$, $P = \{q | q \in L^2(\Omega)\}$

where Ω is the fluid domain, Γ is the boundary of fluid domain which consists of Γ_g and Γ_h, $\boldsymbol{W}$ is a vector corresponding to the momentum weighting function ($\boldsymbol{W} = \sum_i (\alpha_i N_i \boldsymbol{e}_x + \beta_i N_i \boldsymbol{e}_y + \gamma_i N_i \boldsymbol{e}_z)$, where α_i, β_i and γ_i are arbitrary constants, N_i is the shape function for the velocity at ith node point, and $\boldsymbol{e}_x$, $\boldsymbol{e}_y$ and $\boldsymbol{e}_z$ are unit vectors in the x-, y- and z-direction, respectively), q is the weighting function for pressure ($q = \sum_i \lambda_i M_i$, where λ_i is an arbitrary constant and M_i is the shape function for the pressure at ith node point), and $\boldsymbol{n}$ is the unit normal vector outward from the boundary of fluid domain. For time integration, the Crank–Nicolson scheme, which is second-order accurate and unconditionally stable, is to be used.

A. 2. Equation of motion for a circular cylinder

The governing equations for a rigid circular cylinder are Newton's second law for the translational motion,

$$m_p \frac{\mathrm{d}\boldsymbol{V}_p}{\mathrm{d}t} = \boldsymbol{F}_p + \boldsymbol{G}_p \tag{A 6}$$

and the Euler equations for the rotation,

$$I_p \frac{\mathrm{d}\boldsymbol{\omega}_p}{\mathrm{d}t} = \boldsymbol{T}_p, \tag{A 7}$$

where m_p is the mass of the cylinder, I_p is the moment of inertia of the cylinder, $\boldsymbol{V}_p$ ($=[U_p, V_p, W_p]$) is the translational velocity vector of the cylinder, $\boldsymbol{\omega}_p$ is the angular

velocity vector of the cylinder, $\boldsymbol{G}_p$ is the body force exerted by external fields such as gravity, $\boldsymbol{F}_p$ and $\boldsymbol{T}_p$ are the hydrodynamic force and moment acting on the cylinder, respectively. For a circular cylinder of radius a, $m_p = \rho_f \pi a^2$ and $I_p = m_p a^2/2$.

Let Γ_p be the surface of the circular cylinder. Then the hydrodynamic force $\boldsymbol{F}_p$ and moment $\boldsymbol{T}_p$ are obtained by integrating the fluid stress over the cylinder surface,

$$\boldsymbol{F}_p = -\oint_{\Gamma_p} \tilde{\boldsymbol{\sigma}} \cdot \boldsymbol{n} \mathrm{d}\Gamma, \qquad \boldsymbol{T}_p = -\oint_{\Gamma_p} (\boldsymbol{x} - \boldsymbol{X}_p) \times (\tilde{\boldsymbol{\sigma}} \cdot \boldsymbol{n}) \mathrm{d}\Gamma, \tag{A 8}$$

where Γ_p is the boundary of the cylinder surface, $\tilde{\boldsymbol{\sigma}}$ is the traction acting on the fluid along Γ_p and $\boldsymbol{n}$ is the unit normal vector outward from the fluid domain along Γ_p. The centroid $\boldsymbol{X}_p$ and the orientation $\boldsymbol{\Theta}_p$ of the cylinder are updated using a forward Euler finite difference scheme,

$$\boldsymbol{X}_p(t_{n+1}) = \boldsymbol{X}_p(t_n) + \Delta t \boldsymbol{V}_p(t_n), \qquad \boldsymbol{\Theta}_p(t_{n+1}) = \boldsymbol{\Theta}_p(t_n) + \Delta t \boldsymbol{\omega}_p(t_n). \tag{A 9}$$

A. 3. Combined formulation

T. I. Hesla (1991, unpublished note) proposed the *combined formulation* in a fluid–particle system, which incorporates both the fluid and the particle equations of motion in a single coupled variational equation so that the hydrodynamic forces and moments need not be explicitly computed. This comes out naturally, since those fluid forces are internal when the fluid and the structure are considered as one system. The starting point for the combined formulation is equation (A 8), which represents the hydrodynamic force and moment acting on the cylinder. Utilizing the intrinsic feature of the velocity basis function, they can be represented as follows:

$$\left.\begin{aligned} \boldsymbol{F}_p &= -\oint_{\Gamma_p} \tilde{\boldsymbol{\sigma}} \cdot \boldsymbol{n} \, \mathrm{d}\Gamma = -\sum_{i \in \Gamma_p} \oint_{\Gamma_p} N_i (\tilde{\boldsymbol{\sigma}} \cdot \boldsymbol{n}) \, \mathrm{d}\Gamma, \\ \boldsymbol{T}_p &= -\oint_{\Gamma_p} (\boldsymbol{x} - \boldsymbol{X}_p) \times (\tilde{\boldsymbol{\sigma}} \cdot \boldsymbol{n}) \, \mathrm{d}\Gamma = -\sum_{i \in \Gamma_p} \oint_{\Gamma_p} N_i (\boldsymbol{x} - \boldsymbol{X}_p) \times (\tilde{\boldsymbol{\sigma}} \cdot \boldsymbol{n}) \, \mathrm{d}\Gamma. \end{aligned}\right\} \tag{A 10}$$

where N_i is the shape function for the velocity at ith node point on the cylinder surface. On the other hand, using the weak formulation of the Navier–Stokes equations in equation (A 5), the following two equations are readily obtained:

$$\int_\Omega \left[N_i \rho_f \left(\frac{\partial \boldsymbol{u}}{\partial t} + \{(\boldsymbol{u} - \boldsymbol{u}_m) \cdot \nabla\} \boldsymbol{u} \right) + \nabla N_i \cdot \tilde{\boldsymbol{\sigma}} \right] \mathrm{d}\Omega = \oint_\Gamma N_i (\tilde{\boldsymbol{\sigma}} \cdot \boldsymbol{n}) \, \mathrm{d}\Gamma, \tag{A 11}$$

$$(\boldsymbol{x} - \boldsymbol{X}_p) \times \int_\Omega \left[N_i \rho_f \left(\frac{\partial \boldsymbol{u}}{\partial t} + \{(\boldsymbol{u} - \boldsymbol{u}_m) \cdot \nabla\} \boldsymbol{u} \right) + \nabla N_i \cdot \tilde{\boldsymbol{\sigma}} \right] d\Omega = (\boldsymbol{x} - \boldsymbol{X}_p) \times \oint_\Gamma N_i (\tilde{\boldsymbol{\sigma}} \cdot \boldsymbol{n}) \, \mathrm{d}\Gamma. \tag{A 12}$$

Substituting equation (A 11) and equation (A 12) into equation (A 10), one can obtain the following equations:

$$\left.\begin{aligned} \boldsymbol{F}_p &= -\sum_{i \in \Gamma_p} \int_\Omega \left[N_i \rho_f \left(\frac{\partial \boldsymbol{u}}{\partial t} + \{(\boldsymbol{u} - \boldsymbol{u}_m) \cdot \nabla\} \boldsymbol{u} \right) + \nabla N_i \cdot \tilde{\boldsymbol{\sigma}} \right] \mathrm{d}\Omega, \\ \boldsymbol{T}_p &= -\sum_{i \in \Gamma_p} \left\langle (\boldsymbol{x} - \boldsymbol{X}_p) \times \int_\Omega \left[N_i \rho_f \left(\frac{\partial \boldsymbol{u}}{\partial t} + \{(\boldsymbol{u} - \boldsymbol{u}_m) \cdot \nabla\} \boldsymbol{u} \right) + \nabla N_i \cdot \tilde{\boldsymbol{\sigma}} \right] \mathrm{d}\Omega \right\rangle, \end{aligned}\right\} \tag{A 13}$$

where the right-hand sides of equations (A 13) can be obtained from the implicit finite element discretization of the Navier–Stokes equations so that it is not necessary to calculate the hydrodynamic force and moment on the surface of the cylinder explicitly when solving the equations of motion of the cylinder. Finally, substituting equations (A 13) into equation (A 6) and equation (A 7), the following combined formulation for the motion of a cylinder is derived:

$$\left.\begin{aligned} m_p \frac{\mathrm{d}\boldsymbol{V}_p}{\mathrm{d}t} &= -\sum_{i\in\Gamma_p}\int_{\Omega}\left[N_i\rho_f\left(\frac{\partial \boldsymbol{u}}{\partial t}+\{(\boldsymbol{u}-\boldsymbol{u}_m)\cdot\nabla\}\boldsymbol{u}\right)+\nabla N_i\cdot\tilde{\boldsymbol{\sigma}}\right]\mathrm{d}\Omega+\boldsymbol{G}_p,\\ \frac{\mathrm{d}(\boldsymbol{I}_p\boldsymbol{\omega}_p)}{\mathrm{d}t} &= -\sum_{i\in\Gamma_p}\left\langle(\boldsymbol{x}-\boldsymbol{X}_p)\times\int_{\Omega}\left[N_i\rho_f\left(\frac{\partial \boldsymbol{u}}{\partial t}+\{(\boldsymbol{u}-\boldsymbol{u}_m)\cdot\nabla\}\boldsymbol{u}\right)+\nabla N_i\cdot\tilde{\boldsymbol{\sigma}}\right]\mathrm{d}\Omega\right\rangle. \end{aligned}\right\} \tag{A 14}$$

Note that the fluid variables (u, v, p) and the cylinder variables (U_p, V_p, ω_p) are coupled implicitly in the combined formulation. After performing the finite element discretization of equation (A 5) and equations (A 14) with a kinematic constraint, the following form of the global matrix equation for the fluid–structure system can be obtained:

$$\begin{bmatrix} A_{uu} & A_{uv} & B_u & C_{uU_p} & 0 & C_{u\omega_p}\\ A_{vu} & A_{vv} & B_v & 0 & C_{vV_p} & C_{v\omega_p}\\ (B_u)^{\mathrm{T}} & (B_v)^{\mathrm{T}} & 0 & 0 & 0 & 0\\ D_{U_pu} & D_{U_pv} & E_{U_pp} & m_p & 0 & 0\\ D_{V_pu} & D_{V_pv} & E_{V_pp} & 0 & m_p & 0\\ D_{\omega_pu} & D_{\omega_pv} & E_{\omega_pp} & 0 & 0 & I_p \end{bmatrix}\begin{pmatrix} u\\ v\\ p\\ U_p\\ V_p\\ \omega_p \end{pmatrix}=\begin{pmatrix} f_u\\ f_v\\ 0\\ g_{U_p}\\ g_{V_p}\\ g_{\omega_p} \end{pmatrix}, \tag{A 15}$$

where part $[C]$ represents the *kinematic constraint*,

$$[C]=\begin{bmatrix} C_{uU_p} & 0 & C_{u\omega_p}\\ 0 & C_{uV_p} & C_{v\omega_p} \end{bmatrix}$$

which should be satisfied on the surface of the cylinder,

$$\boldsymbol{u}=U_p\boldsymbol{e}_x+V_p\boldsymbol{e}_y+\omega_p\boldsymbol{e}_z\times(\boldsymbol{x}-\boldsymbol{X}_p). \tag{A 16}$$

The global matrix in equation (A 15) is preconditioned by an AILU preconditioner (Nam *et al.* 2002) and solved iteratively by the Bi-CGSTAB (Van der Vorst 1992) solver. To improve the performance of the AILU preconditioner, an efficient variable reordering technique and an element reordering technique using the Cuthill–Mckee algorithm (Saad 1996) are also applied, by which the newly reordered global matrix has a much narrower bandwidth than the original one.

The globally assembled matrix equation (A 15) is solved simultaneously (implicitly). However, note that as in equation (A 9), the position for the cylinder is updated explicitly. For more detailed information of the combined formulation, refer to Hu *et al.* (2001).

A. 4 Mesh refinement

To predict the behaviour of the wake behind a cylinder accurately, the mesh around the cylinder and in the wake region must be fine enough. To do this with a mesh generator without an adaptive technique, a very large number of elements or nodes are required. In the present study, an adaptive technique based on *h*-refinement, which uses shear stress error as *a posteriori* error estimator (Nithiarasu & Zienkiewicz 2000) is used to reduce the number of elements or nodes while resolving the wake flow

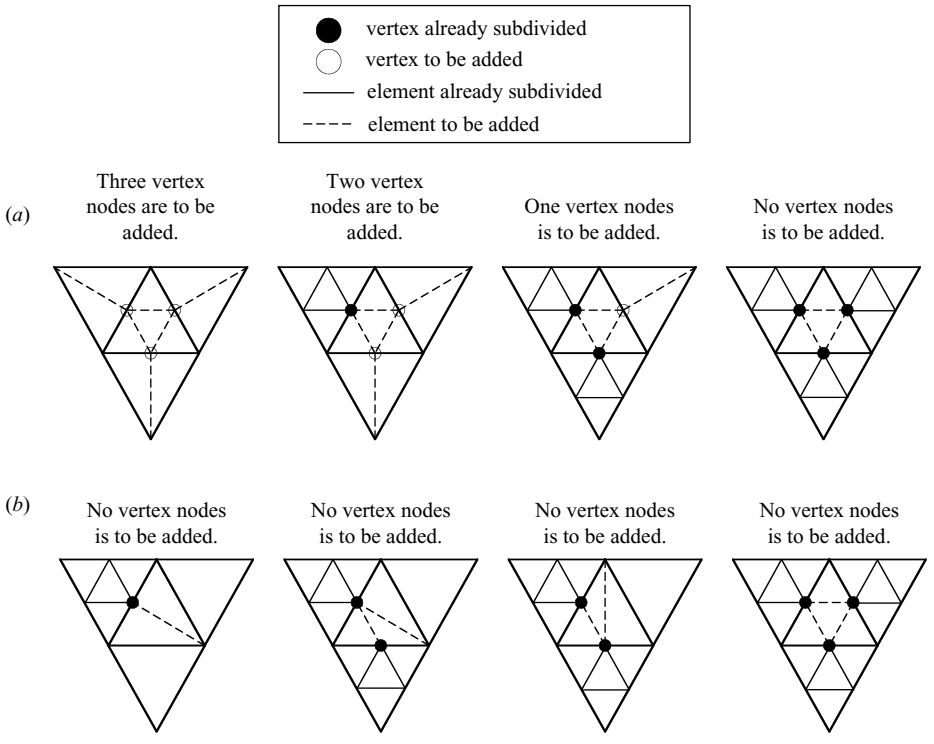

FIGURE 11. Four cases of subdivision when an element (*a*) needs to be subdivided or (*b*) does not need to be divided depending on whether neighboring elements have already been subdivided or not.

accurately. The error in the finite element solution is the difference between the exact and approximate solutions, which can be written for shear stress as follows:

$$\boldsymbol{e}_\tau = \boldsymbol{\tau} - \boldsymbol{\tau}^h, \tag{A 17}$$

where superscript h indicates the finite element solution. As in all problems requiring numerical analysis, since we do not know the exact solution, we need an alternative approximation to it. The trial functions (linear with C_0 continuity) result in a discontinuous approximation of stresses in the present study. The acceptable continuous solution can be obtained by a projection or averaging process in which the stress is assumed to be interpolated using the same function and thus the error in the stresses can now be obtained as

$$\boldsymbol{e}_\tau \approx \boldsymbol{\tau}^* - \boldsymbol{\tau}^h \tag{A 18}$$

where $\boldsymbol{\tau}^*$ is the stress obtained from the projection process (Zienkiewicz & Zhu 1987)

In the present study, we have used the L_2 norm of shear stress error measure as follows:

$$\|\boldsymbol{e}_\tau\| = \left(\int_\Omega \boldsymbol{e}_\tau^{\mathrm{T}} \boldsymbol{e}_\tau \, \mathrm{d}\Omega \right)^{1/2}. \tag{A 19}$$

The above error can be calculated by summing up all the elemental errors as

$$\|\boldsymbol{e}_\tau\|^2 = \sum_{i=1}^{N_{elem}} \|\boldsymbol{e}_\tau\|_i^2 = N_{elem}(\boldsymbol{e}_{avg})^2 \tag{A 20}$$

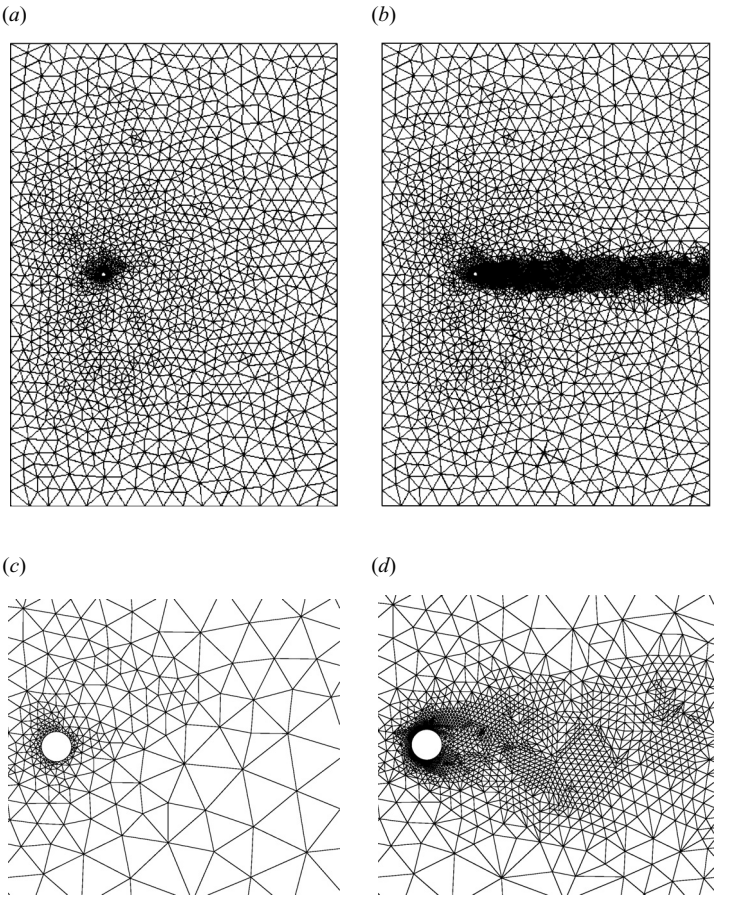

FIGURE 12. (*a*) Initial mesh, (*b*) mesh after 10 refinements, (*c*) close-up view of (*a*), and (*d*) close-up view of (*b*).

where N_{elem} is the total number of elements and e_{avg} is the average error. It is convenient to express the error as a percentage as

$$\eta = \frac{\|\boldsymbol{e}_\tau\|}{\|\boldsymbol{\tau}\|} \times 100(\%) \tag{A 21}$$

where $\|\boldsymbol{\tau}\|$ is the L_2 norm of the shear stress obtained from the projection process.

We use the following form of refinement strategy, which gives a mesh with equal error over every element:

$$h_{new} = h_{old}\frac{\zeta}{E} \tag{A 22}$$

where is ζ the allowed error and E is the element error indicator given by

$$E = \frac{\|\boldsymbol{e}_\tau\|_i}{\|\boldsymbol{\tau}\|} N_{elem}^{1/2}. \tag{A 23}$$

If the new element size predicted by the above procedure is smaller than the old element size, the element is refined. In the present study, it is subdivided into two or three or four elements depending on whether neighbouring elements have already been subdivided. To avoid very small elements, a minimum allowable size is given as input.

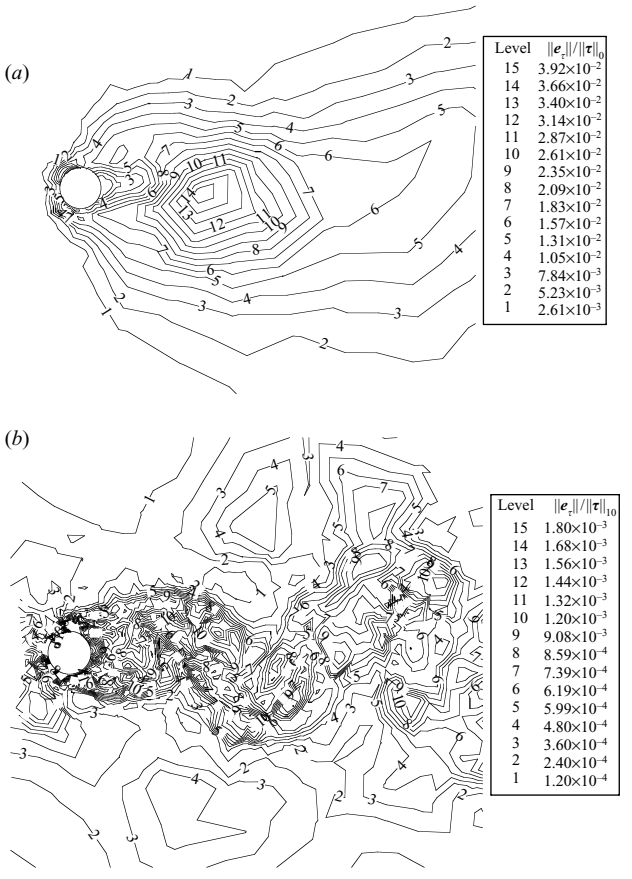

FIGURE 13. Contour plots of error divided by the norm of shear stresss on (*a*) the initial mesh, (*b*) mesh after 10 refinements.

The subdivision schemes used in the present study are shown in figure 11(*a*) and figure 11(*b*). First, vertex nodes in the elements where subdivision is needed, i.e. $h_{new} < h_{old}$, are added and the new elements due to these added vertex nodes, including both the original elements and the neighbouring elements, are numbered as in figure 11(*a*) depending on whether neighbouring elements have already been subdivided. Secondly, elements where subdivision is not needed, i.e. $h_{new} \geqslant h_{old}$, are subdivided and are numbered as in figure 11(*b*) depending on whether neighbouring elements have already been subdivided. After adding vertex nodes where subdivision is needed, mid-nodes are added. The element reordering using Cuthill–Mckee algorithm is performed one more time because the global matrix after the mesh refinement has a much wider bandwidth than that before. An example of mesh refinement is shown figure 12, which shows an initial mesh and the mesh after 10 refinements. It is easily seen in figure 12 that the mesh around the cylinder and in the wake region is refined excellently and the mesh refinement technique works very well. The contour plots of error divided by the norm of the shear stress on the meshes in figures 12(*c*) and 12(*d*) are also shown in figures 13(*a*) and 13(*b*), respectively. Note the difference in the contour levels, i.e. the minimum level of figure 13(*a*) is larger than the maximum level of figure 13(*b*). Note also that the error contours in figure 13(*b*) are very similar to the pattern of vortex shedding. This is quite a natural result considering that the shear stress error was used as *a posteriori* error estimator.

REFERENCES

Billah, K. Y. & Scanlan, R. H. 1991 Resonance, Tacoma narrows bridge failure, and undergraduate physics textbooks. *Am. J. Phys.* **59**, 118–124.

Chen, J.-H., Pritchard, W. G. & TAVENER, S. J. 1995 Bifurcation for flow past a cylinder between parallel planes. *J. Fluid Mech.* **284**, 23–41.

Choi, H. G. 2000 Splitting method for the combined formulation of the fluid-particle problem. *Comput. Meth. Appl. Mech. Engng* **190**, 1367–1378.

Feng, J., Hu, H. H. & Joseph, D. D. 1994 Direct simulation of initial value problems for the motion of solid bodies in a Newtonian fluid: Part 1. Sedimentation. *J. Fluid Mech.* **261**, 95–134.

Fey, U., König, M. & Eckelmann, H. 1998 A new Strouhal-Reynolds-number relationship for the circular cylinder in the range $47 < \sqrt{Re} < 2 \times 10^5$. *Phys. Fluids* **10**, 1547–1549.

Horowitz, M. & Williamson, C. H. K. 2006 Dynamics of a rising and falling cylinder. *J. Fluids Struct.* **22**, 837–843.

Hu, H. H., Joseph, D. D. & Crochet, M. J. 1992 Direct simulation of fluid particle motions. *Theor. Comput. Fluid Dyn.* **3**, 285–306.

Hu, H. H., Patankar, N. A. & Zhu, M. Y. 2001 Direct numerical simulations of fluid-solid systems using the arbitrary Lagrangian-Eulerian technique. *J. Comput. Phys.* **169**, 427–462.

Henderson, R. D. 1997 Nonlinear dynamics and pattern formation in turbulent wake transition. *J. Fluid Mech.* **352**, 65–112.

Jenny, M., Bouchet, G. & Dušek, J. 2003 Nonvertical ascension or fall of a free sphere in a Newtonian fluid. *Phys. Fluids* **15**, L9–L12.

Jenny, M. & Dušek, J. 2004 Efficient numerical method for the direct numerical simulation of the flow past a single light moving spherical body in transitional regimes. *J. Comput. Phys.* **194**, 215–232.

Jenny, M., Dušek, J. & Bouchet, G. 2004 Instabilities and transition of a sphere falling or ascending freely in a Newtonian fluid. *J. Fluid Mech.* **508**, 201–239.

Karamanev, D., Chavarie, C. & Mayer, R. 1996 Dynamics of the free rise of a light solid sphere in liquid. *AIChE J.* **42**, 1789–1792.

Karamanev, D. & Nikolov, L. 1992 Free rising spheres do not obey Newton's law for free settling. *AIChE J.* **38**, 1843–1846.

Nam, Y. S., Choi, H. G. & Yoo, J. Y. 2002 AILU preconditioning for the finite element formulation of the incompressible Navier–Stokes equations. *Comput. Meth. Appl. Mech. Engng* **191**, 4323–4339.

Nithiarasu, P. & Zienkiewicz, O. C. 2000 Adaptive mesh generation for fluid mechanics problems. *Intl J. Numer. Meth. Engng* **47**, 629–662.

Rayleigh, Lord 1945 *The Theory of Sound*, 2nd edn. Vol. II, Section 372. Dover.

Saad, Y. 1996 *Iterative Methods for Sparse Linear Systems*. Boston: PWS Publishing Company.

Strouhal, V. 1878 Uber eine besondere art der tonerregung. *Annalen der Physik und Chemie (Leipzig)*, Neue Folge **Bd.5**, Heft 10, 216–251.

Van Der Vorst, H. A. 1992 Bi-CGSTAB: A fast and smoothly converging variant of Bi-CG for the solution of nonsymmetric linear systems, *SIAM J. Sci. Statist. Comput.* **13**, 631–644.

Veldhuis, C. H. J., Biesheuvel, A. 2007 An experimental study of the regimes of motion of spheres falling or ascending freely in a Newtonian fluid. *Intl J. Multiphase Flow* **33**, 1074–1087.

Veldhuis, C., Biesheuvel, A., van Wijngaarden, L. & Lohse, D. 2005 Motion and wake structure of spherical particles, *Nonlinearity* **18**, C1–C8.

Williamson, C. H. K. 1996 Vortex dynamics in the cylinder wake. *Annu. Rev. Fluid Mech.* **28**, 477–539.

Williamson, C. H. K. & Brown, G. L. 1998 A series in $1/\sqrt{Re}$ to represent the Strouhal-Reynolds number relationship of the cylinder wake. *J. Fluids Struct.* **12**, 1073–1085.

Zienkiewicz, O. C. & Zhu, J. Z. 1987 A simple error estimator and adaptive procedure for practical engineering analysis. *Intl J. Numer. Meth. Engng* **24**, 337–357.

Zovatto, L. & Pedrizzetti, G. 2001 Flow about a circular cylinder between parallel walls. *J. Fluid Mech.* **440**, 1–25.